DOI: 10.1002/ange.201408933

Carbon Dioxide Sorption

Extreme Carbon Dioxide Sorption Hysteresis in Open-Channel Rigid Metal–Organic Frameworks**

*Charl X. Bezuidenhout, Vincent J. Smith, Prashant M. Bhatt, Catharine Esterhuysen, and Leonard J. Barbour**

***Abstract:** A systematic study is presented of three closely related microporous metal-organic frameworks the pore dimensions of which vary according to the choice of 4,4′-bipyridyl linker. The tunable linker allows exploration of the effect of increasing pore dimensions on the sorption behavior of the frameworks. The MOFs described capture CO_2 under supercritical conditions and continue to sequester the gas under ambient conditions. Gas sorption isotherms for CO_2 are compared with thermogravimetric data, and the CO_2 molecules in the channels of the frameworks could be modeled using single-crystal X-ray diffraction analysis. Crystallographic data were used to construct a theoretical model based on DFT methods to calculate framework electrostatic potential maps with a view to understanding the nature of the sorbate–sorbent interactions.*

The potential advantages of metal–organic frameworks (MOFs) for CO_2 capture and storage are derived from a number of their inherent properties. These include chemical versatility, robustness, high thermal and chemical stability, large surface areas, and large void volumes. High guest-accessible volumes and surface areas result in low densities, which in turn may yield high CO_2 sorption capacities by weight. This is evidenced by superior active surface areas per unit weight (up to 7100 $m^2 g^{-1}$ for MOFs)[1] when compared to other sorbents such as activated carbon and zeolites (400 to 1500 $m^2 g^{-1}$). However, for some applications (for example, separation), sorption capacity is less important than selectivity. The latter is influenced by three factors: 1) The molecular sieving effect, which is based on a size/shape exclusion principle; 2) the thermodynamic effect, which results from preferential packing of gas molecules in the pores of the host, the channel topology and the surface interactions between gas molecules, and the channel walls; and 3) the kinetic effect, resulting from different gases having different kinetic diameters and energies, which in turn leads to variation in diffusion rates.[2] Together these factors contribute to the characteristic isotherms associated with sorption; in this regard the IUPAC has classified six typical sorption isotherms (Supporting Information, Figure S1), five of which are based on the work by Brunauer et al. (BDDT system).[3] The type I isotherm is usually associated with microporous frameworks, types II, III, and VI with non-, meso-, or macroporous materials and types V and VI exclusively with mesoporosity. According to Fletcher et al.,[3c] the shapes of the isotherms are influenced by pore size, host–guest, and guest–guest interactions. Moreover, the shapes of the isotherms for rigid frameworks are greatly influenced by electrostatic interactions, which can produce artifacts (for example, adsorption hysteresis and stepped isotherms) similar to those induced by framework flexibility.[3d,e]

Adsorption hysteresis occurs when the sorption and desorption isotherms do not overlap, and it may result from intrinsic framework flexibility, a phase transition, capillary condensation, or gas trapping within the pore apertures.[3a] Sorption isotherms that display hysteresis can be classified into several categories as shown in Scheme 1: extreme (H1 and H4) and intermediate (H2 and H3). In H1 the hysteretic sorption and desorption isotherms are close to vertical and almost parallel to each other, while in H4 they are close to horizontal and almost parallel. Types H2 and H3 have shapes that fall between those of H1 and H4.[3f]

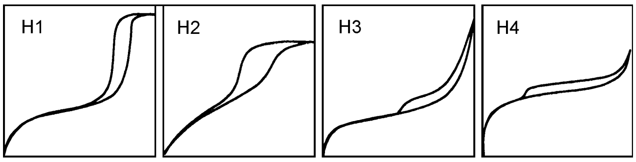

Scheme 1. The four typical hysteretic isotherms.[3f]

The positions of guest molecules in a channel or cavity are determined by steric forces resulting from Pauli repulsion (host–guest fit) and attractive interactions with the walls of the channel or cavity. The latter are primarily due to electrostatic attraction, although dispersion may also play a role. In a largely uniform channel, steric repulsion and attractive dispersion interactions remain relatively constant along the channel length. Thus the electrostatic interactions between the guest and the walls of the channel play a dominant role in determining the guest sorption site.[4] Therefore molecular electrostatic potential (MEP) maps can provide significant insight into the nature of the electrostatic interactions between guest molecules and the host framework.

---

[*] C. X. Bezuidenhout, Dr. V. J. Smith, Dr. P. M. Bhatt,
Prof. C. Esterhuysen, Prof. L. J. Barbour
Department of Chemistry and Polymer Science
University of Stellenbosch, Matieland 7602 (South Africa)
E-mail: ljb@sun.ac.za

[**] L.J.B. and C.E. thank the National Research Foundation (NRF) of South Africa and Stellenbosch University for financial support as well as the Centre for High Performance Computing (CHPC) in Cape Town for the use of their resources.

Supporting information for this article is available on the WWW under http://dx.doi.org/10.1002/anie.201408933.

The MEP ($V(r)$) is a well-established and highly useful method for the study of molecular properties and noncovalent interactions between molecules. Of the various representations of MEPs, the most common are two-dimensional (2D) and three-dimensional (3D) contour maps.[4a,b] The application of MEPs is mainly associated with the study of electrostatic (Coulombic) interactions;[5] for example, in the study of protonation processes,[6] molecular recognition,[7] differentiation between agonists and antagonists,[8] enzyme-ligand interactions,[9] excited electronic states,[10] molecular reactivity,[11] and tautomerization.[12]

The hydrothermal reaction of $Cu(NO_3)_2{\cdot}2.5\,H_2O$, glutaric acid ($gluH_2$), and L_n, where $L_1 = 4,4'$-bipyridine (bpy), $L_2 =$ *trans*-bis(4-pyridyl)ethylene (bpe), and $L_3 = N,N'$-bis(pyridine-4-ylmethylene)hydrazine (bpymh) yielded three 3D MOFs: $[Cu_2(glu)_2(bpy)]{\cdot}2.9\,H_2O$ (**1a**), $[Cu_2(glu)_2(bpe)]{\cdot}3\,H_2O$ (**2a**), and $[Cu_2(glu)_2(bpymh)]{\cdot}7.5\,H_2O$ (**3a**).[13] Green block-shaped crystals of the as-synthesized frameworks were dehydrated by placing them under dynamic vacuum at 150 °C for 24 h, affording crystals of the apohosts **1**, **2**, and **3** (Figure 1). Single-crystal X-ray diffraction analysis (SCD) reveals the homeotypic[14] nature of frameworks **1a**, **2a**, **3a**, **1**, **2**, and **3**. All of the frameworks conform to the monoclinic space group $C2/c$ with their a axes, β angles, unit cell volumes, and channel dimensions responding to changes in the length of the bipyridyl linker. The three rigid microporous frameworks are related to the α-polonium net and contain open 1D corrugated channels with constriction and dilation dimensions of 2.8×5.5 Å and 5.6×7.6 Å for **1**, 4.7×6.5 Å and 7.3×10.9 Å for **2**, and 6.2×7.2 Å and 9.2×10.6 Å for **3**. The framework structures can be described as 2D corrugated layers comprising glutarate anions that are equatorially coordinated to two pentacoordinate Cu cations, thus forming paddlewheel secondary building units (SBUs). Adjacent corrugated layers are joined by the various axially coordinated linkers that form crisscrossed pillars (Supporting Information, Figure S2).

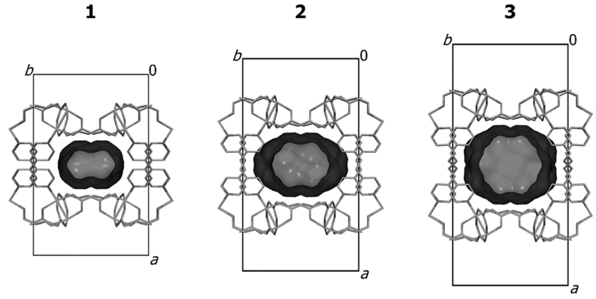

Figure 1. Perspective views along the channels of **1**, **2**, and **3** running parallel to [001]. The guest-accessible surfaces were mapped using a probe of radius 1.4 Å. Hydrogen atoms are omitted for clarity.

We also investigated whether the as-synthesized frameworks could be desolvated under supercritical CO_2 ($scCO_2$) conditions according to a procedure similar to that first reported by Hupp et al.[15] After separately exposing **1a**, **2a**, and **3a** to $scCO_2$ for 24 h, crystals of suitable quality were selected under ambient conditions and then subjected to SCD analysis at 100 K. The crystal structures reveal that the original H_2O molecules had been replaced by CO_2 molecules, which are then retained in the channels after removal of the crystals from $scCO_2$. The new phases **1b**, **2b**, and **3b** are also homeotypic with respect to the as-synthesized and apohost phases.

In all three cases, it was possible to model the CO_2 molecules in the dilated regions of the channels using SCD analysis (Figure 2); guest arrangements in the channels of **1b**, **2b**, and **3b** resemble two of those observed in dry ice: that is, slipped-parallel and crossed (Supporting Information, Figure S3). However, the T-shaped motif is not observed. The intermolecular distances between neighboring CO_2 molecules are much larger than those observed in dry ice, and this is most likely due to corrugation of the channel.

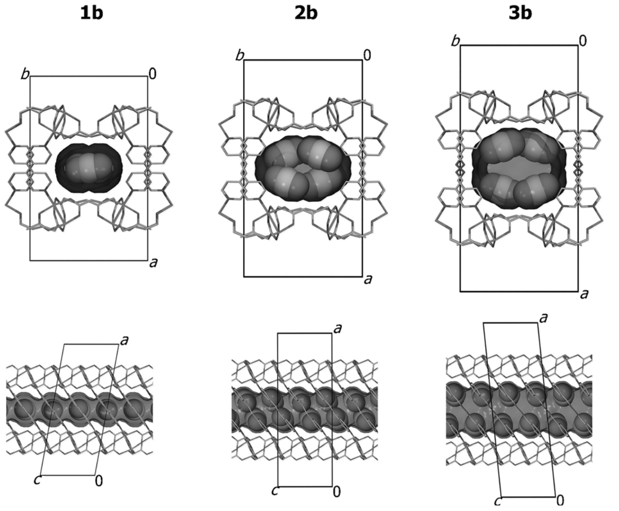

Figure 2. Perspective views along [001] (top) and [010] (bottom) of the crystal structures obtained for **1b**, **2b**, and **3b** after $scCO_2$ treatment.[17] The CO_2 molecules are shown in space-filling representation, and the solvent-accessible surfaces were mapped with a probe of radius of 1.4 Å. Hydrogen atoms are omitted for clarity.

To distinguish between the idealized arrangements of CO_2 molecules in dry ice and those observed in frameworks **1b**, **2b**, and **3b**, we prefix the term describing the arrangement with "pseudo". The CO_2 molecules in **1b** are pseudo-crossed along the channel while those in **2b** are both pseudo-crossed along the channel and pseudo-slipped-parallel diagonally across the channel (Supporting Information, Figure S3). The CO_2 molecules of **3b** only adopt the pseudo-slipped-parallel arrangement diagonally across the channel.

Owing to the remarkable stability of **1b**, **2b**, and **3b** to guest-loss under ambient conditions, it was possible to analyze each sample using thermogravimetric analysis (TGA; Figure 3), differential scanning calorimetry (DSC), and Fourier transform infrared (FTIR) spectroscopy. Comparative FTIR analysis of the as-synthesized, activated, and $scCO_2$-exposed materials confirmed the presence of CO_2 in **1b**, **2b**, and **3b** (Supporting Information, Figure S4). The evolution ranges for the guest CO_2 in the three frameworks are 40–260 °C for **1b**, 30–90 °C for **2b**, and 30–80 °C for **3b** (Support-

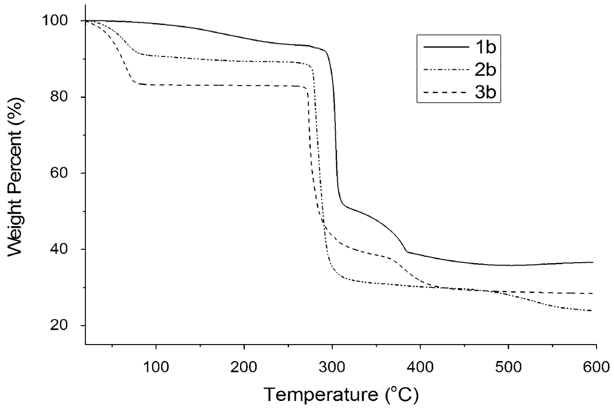

Figure 3. TGA thermograms for **1 b**, **2 b**, and **3 b**.

ing Information, Figure S5; stoichiometric data obtained from TGA and SQUEEZE[16] calculations are tabulated in Table S1). Thermal stability, defined here as the temperature corresponding to the maximum rate of expulsion of CO_2 from the framework, is inversely related to the size of the channel, with **1 b** ≫ **2 b** ≈ **3 b** (164, 66, and 64 °C, respectively), implying that CO_2 evolution follows a trend of decreasing steric stabilization.

The isotherms shown in Figure 4 are characteristically type I, as expected for microporous frameworks.[3b] Furthermore, all three isotherms exhibit hysteresis, with **1** and **2** displaying a combination of H1 (0 to 7 bar) and H4 (7 to 30 bar) extreme hysteresis, while **3** displays only type H4 hysteresis. For each isotherm we have calculated the extent of hysteresis (as defined in the Supporting Information, and specifically for use in this work), which is expressed as a percentage. The isotherm for **2** exhibits the most extreme hysteresis (21.1 %), followed by **1** (13.1 %) and **3** (3.3 %). It is interesting to note that framework **2**, with intermediate channel dimensions, experiences the most extreme hysteresis, while the order of hysteresis experienced by **1** and **3** corresponds inversely to their relative channel dimensions.

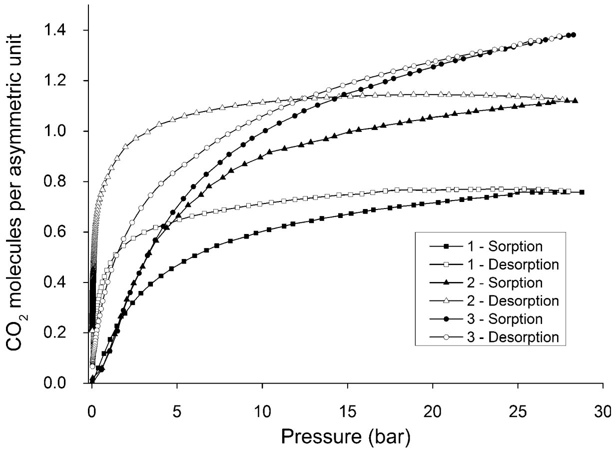

Figure 4. Type I CO_2 sorption and desorption isotherms, measured at 25 °C, for frameworks **1**, **2**, and **3**.

The results for **2** are also at odds with the thermal stability data determined from TGA, and a computational investigation was therefore undertaken to explain this apparent anomaly.

The unusual hysteretic behavior of **2** cannot be explained by steric interactions (that is, channel topology) alone. We therefore investigated the host–guest electrostatic interactions to quantify the stability of CO_2 in frameworks **1**, **2**, and **3**. For each framework, the electrostatic potential (FEP) was calculated based on a channel three unit cells in length along [001] (Supporting Information, Figure S6). Using electron density data obtained from DFT calculations (see the Supporting Information for details), three-dimensional electron density contours at 0.01 e^- $Å^{-3}$ intervals were calculated for both the CO_2 molecules and the framework channels. The electrostatic potential calculated for each framework was then mapped onto the two electron density contours for each host–guest system (Figure 5). From the channel electron density contours, it appears that the three frameworks have similar electrostatic topologies. To elucidate how this influences the CO_2 molecules, the FEPs were mapped onto the CO_2 electron density contours in their crystallographically determined positions. For comparison, the molecular electrostatic potential of an isolated CO_2 molecule is shown at the bottom left of Figure 5; negative potentials are present on the oxygen atoms and, consequently, a highly positive potential is centered on the carbon atom. This suggests that a CO_2 carbon atom can form stronger electrostatic interactions as compared to the oxygen atoms.

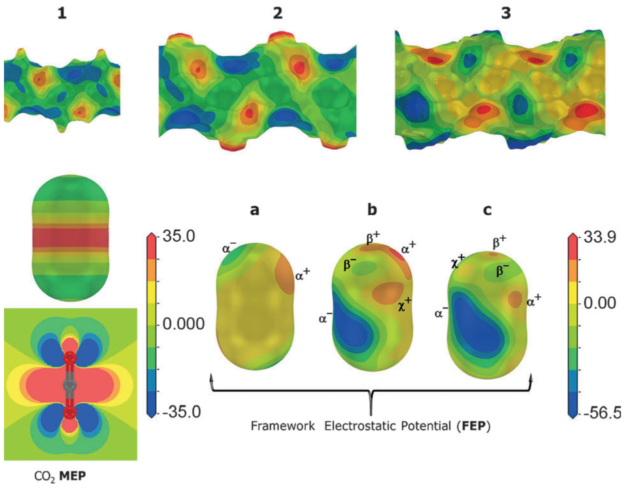

Figure 5. FEP surfaces of **1**, **2**, and **3** mapped onto their respective 0.01 e^- $Å^{-3}$ electron density contours. Bottom left: The molecular electrostatic potential (MEP) of an isolated CO_2 molecule mapped onto the 0.01 e^- $Å^{-3}$ electron density contour (upper) and a 2D slice of the CO_2 electrostatic potential (lower). Bottom right: FEP surfaces of a) **1**, b) **2**, and c) **3** mapped onto the 0.01 e^- $Å^{-3}$ electron density contours of the CO_2 molecule in their crystallographic locations. The gradation on the scale bar is in kcal mol^{-1}, with positive values in red and negative values in blue.

The significance of the electrostatic potential becomes apparent when we consider the Coulombic interactions between CO_2 molecules and the three frameworks. The FEPs of **1**, **2**, and **3** mapped onto the CO_2 molecules provide a detailed representation of their electrostatic interactions with the frameworks. Attractive interactions between the CO_2 molecules and the surrounding framework occur where the MEPs and FEPs display opposite coloring (in the extreme, blue on red). The bottom right-hand side of Figure 5 shows that **1** possesses moderate positive and negative potentials near the oxygen atoms of the CO_2 molecules, as well as a weak positive potential around the carbon atom. As there is little overall electrostatic stabilization between the CO_2 molecules and the host framework, the CO_2 is mostly stabilized by dispersion interactions (London forces). Frameworks **2** and **3** have strong negative potentials (almost double the magnitude of those of their positive potentials; Supporting Information, Table S2) near the carbon atom of the CO_2 molecule (Figure 5, blue regions). These strong electrostatic interactions therefore determine the positions of the CO_2 molecules within the frameworks of **2** and **3**. Further fine-tuning of the CO_2 position and orientation is achieved through weaker electrostatic interactions between the framework and the oxygen atoms of the CO_2 molecules. The only destabilizing electrostatic interactions in **2** and **3** are due to negative potentials on the oxygen atoms of the CO_2 molecules that are repelled by the negative potentials β^- and χ^- for their respective frameworks (Supporting Information, Table S2). Framework **3** has a slightly larger value for the negative potential α^-, thus forming a more stabilizing interaction with the positive potential on the CO_2 as compared to **2**, while β^- and χ^- for **2** are far lower in magnitude than those for **3** (indicating lower electrostatic repulsion and hence less destabilization). Moreover, **2b** shows the largest positive potentials around the oxygen atoms of the CO_2, confirming that framework **2** possesses the most electrostatically stabilized site for CO_2 binding. All of the positive FEP maxima are due to framework hydrogen atoms, while the FEP minima are due to the carboxylate oxygen atoms (Supporting Information, Figure S7). The guest docking sites in **2** and **3** thus appear to be electrostatically complementary to CO_2 molecules. In **1**, the CO_2 molecules are bound sterically, whereas those in **2** and **3** are able to adjust their positions in accordance with the electrostatics of the framework, thereby maximizing host–guest interactions.

In summary, we have shown that open-channeled MOFs are capable of trapping CO_2 under $scCO_2$ conditions while also being able to sequester CO_2 at room temperature (RT). These MOFs display extreme hysteresis at high pressures and RT, and we have shown that framework electrostatic maps (FEPs) provide a powerful means of understanding trends in host–guest binding stability. We have shown that MOFs **1**, **2**, and **3** meet two of the three principles of selectivity mentioned earlier: 1) The size/shape exclusion principle and 2) the thermodynamic effect owing to preferential packing, surface interactions, and suitable topology. The third principle (the kinetic effect) is a property of the gas and not of the framework. From our test-case study of three analogous frameworks, we can conclude that the steric and electrostatic topologies of framework **2** provide the most favorable combination of factors for binding CO_2 guest molecules, thus explaining the observed extreme sorption-desorption hysteresis.

Received: September 9, 2014

Keywords: carbon dioxide sorption · extreme hysteresis · framework electrostatic potential · high-pressure sorption · molecular electrostatic potential

---

[1] D. M. D'Alessandro, B. Smit, J. R. Long, *Angew. Chem. Int. Ed.* **2010**, *49*, 6058–6082; *Angew. Chem.* **2010**, *122*, 6194–6219.

[2] a) Y. S. Bae, R. Q. Snurr, *Angew. Chem. Int. Ed.* **2011**, *50*, 11586–11596; *Angew. Chem.* **2011**, *123*, 11790–11801; b) K. Sumida, D. L. Rogow, J. A. Mason, T. M. McDonald, E. D. Bloch, Z. R. Herm, T. H. Bae, J. R. Long, *Chem. Rev.* **2012**, *112*, 724–781; c) Y. Peng, V. Krungleviciute, I. Eryazici, J. T. Hupp, O. K. Farha, T. Yildirim, *J. Am. Chem. Soc.* **2013**, *135*, 11887–11894.

[3] a) V. Gold in *Compendium of Chemical Terminology*, 2nd ed. (Eds.: A. D. McNaught, A. Wilkinson), Blackwell Scientific Publications, Oxford, **1997**, p. 585; b) S. Brunauer, L. Deming, W. Deming, E. Teller, *J. Am. Chem. Soc.* **1940**, *62*, 1723–1732; c) A. J. Fletcher, K. M. Thomas, M. J. Rosseinsky, *J. Solid State Chem.* **2005**, *178*, 2491–2510; d) J. T. Culp, M. R. Smith, E. Bittner, B. Bockrath, *J. Am. Chem. Soc.* **2008**, *130*, 12427–12434; e) K. S. Walton, A. R. Millward, D. Dubbeldam, H. Frost, J. J. Low, O. M. Yaghi, R. Q. Snurr, *J. Am. Chem. Soc.* **2008**, *130*, 406–407; f) M. D. Donohue, G. L. Aranovich, *J. Colloid Interface Sci.* **1998**, *205*, 121–130.

[4] a) Q. Yang, C. Zhong, *ChemPhysChem* **2006**, *7*, 1417–1421; b) Q. Yang, D. Liu, C. Zhong, J. Li, *Chem. Rev.* **2013**, *113*, 8261–8323; c) Q. Yang, Q. Xu, B. Liu, C. Zhong, S. Berend, *Chin. J. Chem. Eng.* **2009**, *17*, 781–790.

[5] a) S. Demir, M. Dinçer, A. Cukurovali, I. Yilmaz, *Int. J. Quantum Chem.* **2012**, *112*, 1016–1028; b) J. S. Murray, P. Politzer, *WIREs Comput. Mol. Sci.* **2011**, *1*, 153–163; c) G. Náray-Szabó, G. G. Ferenczy, *Chem. Rev.* **1995**, *95*, 829–847.

[6] a) R. Bonaccorsi, J. Tomasi, E. Scrocco, A. Pullman, *Chem. Phys. Lett.* **1972**, *12*, 622–624; b) R. Bonaccorsi, A. Pullman, E. Scrocco, J. Tomasi, *Theor. Chim. Acta* **1972**, *24*, 51–60; c) I. Tuñón, E. Silla, J. Tomasi, *J. Phys. Chem.* **1992**, *96*, 9043–9048; d) J. S. Murray, P. Lane, M. Göbel, T. M. Klapötke, P. Politzer, *J. Chem. Phys.* **2009**, *130*, 104304.

[7] a) E. P. Bishop, R. Rohs, S. C. J. Parker, S. M. West, P. Liu, R. S. Mann, B. Honig, T. D. Tullius, *ACS Chem. Biol.* **2011**, *6*, 1314–1320; b) A. Chang, B. A. Hackett, C. C. Winter, U. J. Buchholz, R. E. Dutch, *J. Virol.* **2012**, *86*, 9843–9853; c) F. S. Dukhovich, M. B. Darkhovskii, *J. Mol. Recognit.* **2003**, *16*, 191–202; d) P. Sjoberg, J. S. Murray, T. Brinck, P. Evans, P. Politzer, *J. Mol. Graph.* **1990**, *8*, 81–85.

[8] a) I. Alkorta, H. O. Villar, *J. Med. Chem.* **1994**, *37*, 210–213; b) N. El Tayar, P. A. Carrupt, H. Van de Waterbeemd, B. Testa, *J. Med. Chem.* **1988**, *31*, 2072–2081.

[9] a) M. Negri, M. Recanatini, R. W. Hartmann, *J. Comput.-Aided Mol. Des.* **2011**, *25*, 795–811; b) J. E. Mendieta-Wejebe, M. C. Rosales-Hernández, H. Rios, J. Trujillo-Ferrara, G. López-Pérez, F. Tamay-Cach, R. Ramos-Morales, J. Correa-Basurto, *J. Mol. Model.* **2008**, *14*, 537–545.

[10] a) M. K. Shukla, A. Kumar, P. C. Mishra, *J. Mol. Struct.* (*Theochem*) **2001**, *535*, 269–277; b) D. M. Upadhyay, M. K. Shukla, P. C. Mishra, *J. Mol. Struct.* (*Theochem*) **2000**, *531*, 249–266.

[11] a) K. Kádas, S. Kugler, G. Náray-Szabó, *J. Phys. Chem.* **1996**, *100*, 8462–8467; b) I. Alkorta, J. J. Perez, H. O. Villar, *J. Mol. Graph.* **1994**, *12*, 3–13.

[12] M. Adrover, C. Caldés, B. Vilanova, J. Frau, J. Donoso, F. Muñoz, *New J. Chem.* **2012**, *36*, 1751 – 1761.

[13] a) B. Chen, Y. Ji, M. Xue, F. R. Fronczek, E. J. Hurtado, J. U. Mondal, C. Liang, S. Dai, *Inorg. Chem.* **2008**, *47*, 5543 – 5545; b) R. Dey, R. Haldar, T. K. Maji, D. Ghoshal, *Cryst. Growth Des.* **2011**, *11*, 3905 – 3911; c) B. Rather, M. J. Zaworotko, *Chem. Commun.* **2003**, 830 – 831.

[14] L. J. Barbour, D. Das, T. Jacobs, G. O. Lloyd, V. J. Smith, *Supramolecular Chemistry: From Molecules to Nanomaterials*, Wiley, Hoboken, **2012**.

[15] A. P. Nelson, O. K. Farha, K. L. Mulfort, J. T. Hupp, *J. Am. Chem. Soc.* **2009**, *131*, 458 – 460.

[16] PLATON, *A Multipurpose Crystallographic Tool*, Utrecht University: Utrecht, The Netherlands, **2008**.

[17] CCDC 1016695 (**1a**), 1016696 (**1b**), and 1016697 (**1c**) contain the supplementary crystallographic data for this paper. These data can be obtained free of charge from The Cambridge Crystallographic Data Centre via www.ccdc.cam.ac.uk/data_request/cif.